Chinese Chemical Letters 34 (2023) 107411

Contents lists available at ScienceDirect

Chinese Chemical Letters

journal homepage: www.elsevier.com/locate/cclet

Tuning the structures of polypyridinium salts as bifunctional cathode interfacial layers for all-solution-processed red quantum-dot light-emitting diodes

Shuguang Fu[a], Xiaojun Yin[a,*], Yang Tang[b], Guohua Xie[b,*], Chuluo Yang[a,*]

[a] Shenzhen Key Laboratory of New Information Display and Storage Materials, College of Materials Science and Engineering, Shenzhen University, Shenzhen 518060, China

[b] Hubei Key Lab on Organic and Polymeric Optoelectronic Materials, Department of Chemistry, Wuhan University, Wuhan 430072, China

ARTICLE INFO

Article history:
Received 26 January 2022
Revised 24 March 2022
Accepted 6 April 2022
Available online 11 April 2022

Keywords:
Self-doping
Cathode interfacial layer
QLED
Pyridinium salts
All-solution-processable

ABSTRACT

Self-doping cathode interfacial layers (CILs) with both favorable electron injection and transport characteristics meet the key requirement for realizing high-performance optoelectronic devices with simplified structures. Herein, four different polypyridinium salts with tunable backbones, side chains and counterions are elaborately designed to afford them desirable film-forming property, polarity, structural rigidity and self-doping feature. All-solution-processed red quantum dot light-emitting diodes (QLEDs) employing them as bifunctional CILs render remarkably improved device performances in contrast to the typical CIL material of poly[(9,9-bis(30-(*N*,*N*-dimethylamino)propyl)-2,7-fluorene)-*alt*-2,7-(9,9-dioctylfluorene)] (PFN). The maximum external quantum efficiency of 2.74% achieved in this work represents one of the best values among the all-solution-processed QLEDs with individual organic CILs.

Luminophores with high color purity and accurate color tunability are urgently needed to meet the necessity requirements of high-quality displays and colorful lighting [1–4]. Typical organic emitters, including phosphors and thermally activated delayed fluorophors, are conventionally suffer from large vibrational relaxation at their excited states, resulting in significantly broadened full-width at half-maximum (FWHM) [5–7]. Molecular design concepts with the separated distributions of the lowest unoccupied molecular orbital (LUMO) and the highest occupied molecular orbital (HOMO) on single atoms proposed a valid approach to generate multiple resonance emitters with a FWHM < 40 nm [8,9]. Nevertheless, the complicated synthetic routes and serious aggregation-caused quenching restrained the arbitrarily application in some scenario. Utilizing quantum confinement effects in colloidal inorganic semiconductor nanocrystals deliver an alternative strategy to address these concerns [10–12], since the inherent photophysical stability, high photoluminescent quantum yield, size-tunable emission wavelength, and narrow emission line-widths enable them as ideal candidates to high-performance quantum dot light-emitting diodes (QLEDs) [13–16]. To fully realize the superiority of QLEDs, endeavors including developing novel quantum dots (QDs) with versatile structures and applicable transport materials with favorable charge injection/transport abilities should be taken into account synchronously [17–20].

All-solution-processed optoelectronic devices are compatible with low-cost mass production and versatility in realizing large-area flexible devices, which suffice the energy-saving and diverse demands of display [21–23]. QDs are one of typical solution-processable inorganic or organic/inorganic hybrid semiconductor nanocrystals [24]. However, the stacking of multilayer organic functional materials is particularly challenging due to the critical problem of solvent selection, and the electron injection/transporting layers in most QLEDs were deposited *via* vacuum deposition, which bring about additional energy-intensive processes [25–27]. Alternatively, the incorporation of inorganic metal oxide (*e.g.*, ZnO) or alloyed (*e.g.*, $Zn_{1-x}Mg_xO$, $0 \leq x \leq 1$) nanoparticles that dispersed in alcoholic solutions engage an accessible strategy to satisfy the orthogonal solvent rule [28–32]. Fatally, the imbalanced electron injection/transporting of the metal oxides tend to cause deteriorative nonradiative recombination. Especially, the high brittleness nature dramatically limits their application in flexible devices [33–35]. Developing water/alcohol soluble polymeric cathode interfacial layers (CILs) can fully release the potential of QLED. However, the commonly used CILs exhibited poor electrical properties and thus resulted in inferior device performances. For in-

* Corresponding authors.
E-mail addresses: xiaojunyin@szu.edu.cn (X. Yin), guohua.xie@whu.edu.cn (G. Xie), clyang@szu.edu.cn (C. Yang).

https://doi.org/10.1016/j.cclet.2022.04.009
1001-8417/

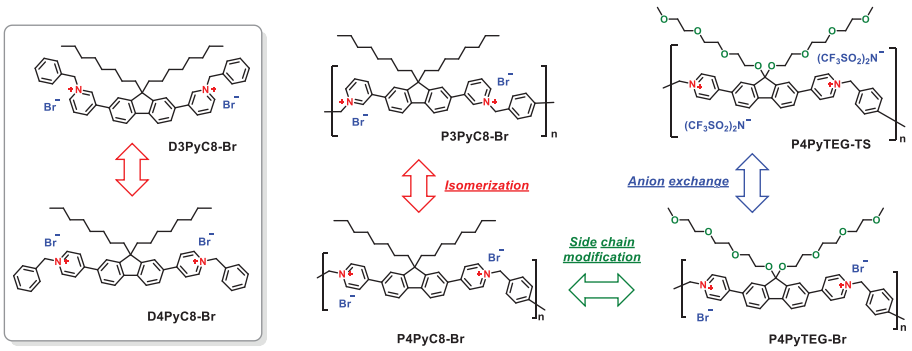

Scheme 1. Chemical structures of these investigated pyridinium salts.

stance, Son *et al.* employing polyethylenimine ethoxylated (PEIE) as CILs together with CdSe@ZnS QD emitters only achieved a low external quantum efficiency (η_{ext}) of 0.39% [36,37]. Recently, Brovelli and co-workers reported a series of polyfluorene based CILs with polar side chains realized a significantly improved η_{ext} up to 6.1% at deep-red region (650 nm) [38]. Meanwhile, the inserting of low work-function metal barium basically reduced the stability of devices. Therefore, it is urgent but challenging to gain desirable water/alcohol soluble polymers with combination of both high electron injection and transporting properties. Self-doping CILs, as demonstrated in our previously works, unfolded a robust concept to alleviate these problems whereby anion-induced electron transfer (AIET) between electron-rich anions and electron-deficient π-conjugated quaternary ammonium cations [39–41].

In this work, four π-conjugated polypyridinium salts with tunable backbones, side chains and counter-ions were designed and synthesized (Scheme 1). As expected, all the four polypyridinium salts reveal typical self-doping feature according to the electron paramagnetic resonance (EPR) results. The photophysical and electrochemical studies demonstrated that the structural relaxations at excited states can be largely restricted by altering the N^+ atoms to the *para*-positions, which was further elucidated by theoretical simulations. In addition, other key parameters including surface morphology and polarity were delicately manipulated along with the varying of side-chains or counter-ions, delivering the desirable CILs. Using these polypyridinium salts as bifunctional electron injection/transport layers, the all-solution-processed red QLED exhibited remarkably improved device performances in contrast to the commercially available CILs of poly[(9,9-bis(30-(*N*,*N*-dimethylamino)propyl)−2,7-fluorene)-*alt*-2,7-(9,9-dioctylfluorene)] (PFN). For example, at the same bias voltage of 4 V, the current density of the device based on P4PyTEG-TS (5.194 mA/cm^2) is 45 times higher than that of the device with PFN (0.115 mA/cm^2), and the maximum η_{ext} of 2.74% achieved by P4PyC8-Br is 1.5 times higher than that of the PFN based device (1.83%), among the best results of all-solution-processed QLED with the organic CILs. In addition, these polypyridinium salts incorporated devices exhibited small efficiency roll-off with only 10% reduction (η_{ext}) even at a very high current density of 100 mA/cm^2.

The synthesis routes of these investigated pyridinium salts were depicted in Scheme S1 (Supporting information). Firstly, the key monomers of pyridine-substituted fluorenes were obtained from Suzuki cross-coupling reaction between the 2,7-dibromofluorene derivates and corresponding pyridineboronic acid with the considerable yields over 75%. Subsequently, quaternization with the 1,4-bis(bromomethyl)benzene gave different polypyridinium bromides (P3PyC8-Br, P4PyC8-Br and P4PyTEG-Br), and an additional ion-exchange with bistrifluoromethanesulfonimide (TS^-) lithium salt yielded P4PyTEG-TS. All these polypyridinium salts were well identified with ^{1}H NMR (Figs. S1–S6 in Supporting information), ^{13}C NMR and gel permeation chromatography, and the self-doping properties were identified with EPR measurements. Notably, all these polypyridinium salts demonstrate favorable solubility in polar solvent, such as, methanol (MeOH) and dimethyl formamide (DMF), which meet the requirement of solvent selectivity in multi-layered all-solution-processed QLEDs.

UV–vis absorption and photoluminescence (PL) spectra of these polypyridinium salts both in dilute MeOH and films were collected (Fig. S7 in Supporting information). To highlight the diversity derived from N^+ positions, pyridinium dibromides (D3PyC8-Br and D4PyC8-Br, Scheme 1) were synchronously synthesized and the relevant spectra were measured in parallel. As shown in Figs. S7a and b, in comparison with the D4PyC8-Br, significant peak shifts from dilute MeOH to aggregated thin film states can be observed from both absorption and emission spectra of D3PyC8-Br. Meanwhile, a larger Stokes shift of 8751 cm^{-1} (*vs.* 3570 cm^{-1}) in MeOH, and 5124 cm^{-1} (*vs.* 4561 cm^{-1}) in film were calculated for D3PyC8-Br (*vs.* D4PyC8-Br), respectively. Such phenomena are more pronounced in polypyridinium bromides (Figs. S7c and d), which indicating the structural relaxations at excited states can be considerably restricted by altering the N^+ atoms to the *para*-positions. In addition, all the polypyridinium salts exhibited inconspicuous solvation effect according to their polarity dependence absorption and photoluminescence spectra (Figs. S8 and S9 in Supporting information), revealing a typical locally excited state transition. As shown in Fig. S7g, a reversible reduction process was recognized from the cyclic voltammetry (CV) curve of D4PyC8-Br, reflecting a more efficient electron transfer channel of D4PyC8-Br than D3PyC8-Br. Compared with P4PyC8-Br, the negligible changes of absorption and PL spectra were identified with the changes of side-chains (Fig. S7e) or counter-ions (Fig. S7f). The LUMO levels of these polypyridinium salts were estimated as −3.56, −3.63, −3.61 and −3.62 for P3PyC8-Br, P4PyC8-Br, P4PyTEG-Br, and P4PyTEG-TS, respectively (Table S1 in Supporting information), ensuring a suitable affinity for electron injection.

To well understand the significance of isomerization, side-chain modification and counter anions, density functional theory (DFT) calculations employing Gaussian 16 were performed. Figs. 1a–d displayed the HOMO and LUMO distributions of these monomers. Obviously, the HOMOs of these pyridinium bromides were largely localized at the electron-rich Br^- anions and affording the similar HOMO levels at around −5.13 eV. However, the LUMO distributions of the three bromides exhibited the significant difference, *i.e.*, the LUMOs of D3PyC8-Br were mainly delocalized at the unilateral pyridinium moieties, while the LUMOs were scattered across the whole π-delocalization area when the N^+ atoms shift to the *para*-position of fluorenyl (D4PyC8-Br and D4PyTEG-Br), resulting in the slightly reduced LUMO levels from −2.60 to −2.82 and −2.72 eV, respectively. Due to the poor electron donating ability

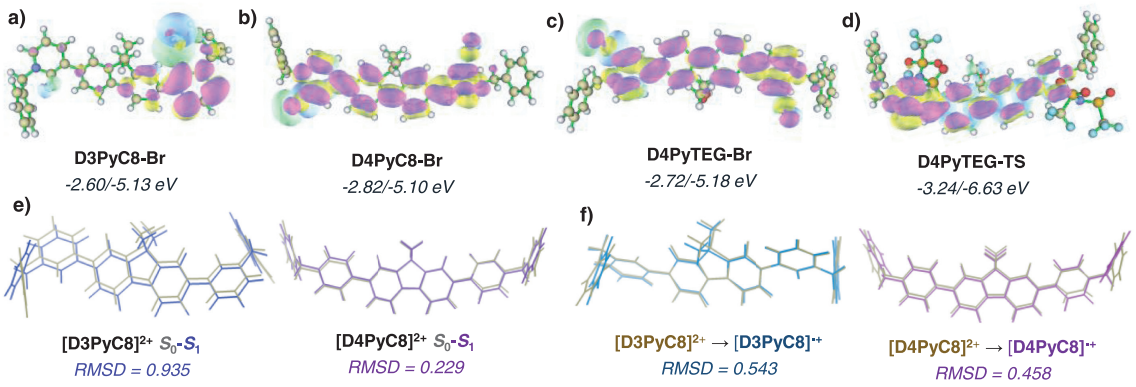

Fig. 1. HOMO (cyan/prasinous) and LUMO (purplish/yellow) distributions for (a) D3PyC8-Br, (b) D4PyC8-Br, (c) D4PyTEG-Br, and (d) D4PyTEG-TS, respectively. The comparison diagrams of optimized geometrical configurations of $[D3PyC8]^{2+}$ and $[D4PyC8]^{2+}$ at different states, for (e) $S_0 \rightarrow S_1$ and (f) divalent cationic state to corresponding reduction state.

of TS^-, both HOMOs and LUMOs of D4PyTEG-TS were distributed over the whole fluorenyl pyridinium skeleton together with the remarkably descended HOMO/LUMO levels of −6.63/−3.24 eV, respectively. Considering the significant difference of photophysical and electrochemical behaviors between P3PyC8-Br and P4PyC8-Br, geometric changes of the π-conjugated pyridinium divalent cations from ground states (S_0) to the corresponding excited states (S_1) or reduction states were calculated and analyzed with Multiwfn 3.8 [42]. As shown in Fig. 1e, the calculated root-mean-square deviations (RMSDs) for $[D3PyC8]^{2+}$ cation (0.935 Å) is remarkably higher than that of $[D4PyC8]^{2+}$ (0.229 Å), indicating a more dramatical structural relaxation during the photoexcitation process ($S_0 \rightarrow S_1$) of the former than the latter. The same trend can be observed on the electron transfer process (*i.e.*, reduction) as well, and the calculated RMSDs from S_0 to the corresponding reduction states were 0.543 and 0.458 Å for $[D3PyC8]^{2+}$ and $[D4PyC8]^{2+}$ (Fig. 1f), respectively, which reflected a more convenient electron transport backbone of the latter than the former.

To explore the self-doping and electron transfer characteristics of these polypyridinium salts, EPR measurements either in dark or under ultraviolet excitation were implemented. As displayed in Fig. 2, all these polypyridinium salts display positive EPR signals in dark with *g* values ~2.004 (Table S1), indicating the existence of free radical anions and affording them n-type self-doping. Nevertheless, the EPR intensity of P3PyC8-Br and P4PyC8-Br were obviously higher than those of P4PyTEG-Br and P4PyTEG-TS, which can be attributed to the deeper HOMO levels of the latter than the former, and leading to weaker anion-π interactions [39]. Meanwhile, with the excitation of UV-light, all these polypyridinium salts demonstrated evident enhancement of EPR intensity originating from the photoinduced electron transfer (PET) mechanism [7]. Notably, the self-doping characteristics enable them as suitable candidates for the better interfacial energy-level alignment and the unobstructed PET process implying the favourable electron transfer property, which is crucial for developing state-of-the-art CILs [43].

Figs. S10a–d (Supporting information) displayed the atomic force microscope (AFM) images of these polypyridinium salts. Noticeably, the root-mean-square (RMS) roughness values of these films were mainly relying on the sites of N^+, side-chains, and counter-ions either. In comparison with the RMS of P3PyC8-Br in film (4.30 nm), the significantly decreased RMS of P4PyC8-Br (1.89 nm) along with the N^+ atoms switching to the *para*-position was observed, which can be ascribed to the linear extension of P4PyC8-Br. In addition, the film-forming property of P4PyTEG-Br can be further improved by altering the hydrophobicity alkyl side chains to hydrophilicity oxyalkyl chains, yielding a smaller RMS of 0.43 nm. While, the ion-exchange with large-sized TS^- (P4PyTEG-TS) will result in an increase of roughness (RMS = 2.08 nm) instead. The contact angles between the polypyridinium surfaces and the water drops were remarkably changed with different side chains and anions (Fig. S10e in Supporting information). With the replacement of hydrophilicity oxyalkyl chains, the contact angles dropped sharply from 54.86° (P4PyC8-Br) to 11.93° (P4PyTEG-Br). However it turned back to 64.75° when modified with hydrophobicity TS^- counter-ions.

To investigate the energy transfer and exciton quenching between the CILs and the red QD (QD-R) emitting layers, the transient PL decay profiles of these samples were measured. As revealed in Fig. S11 and Table S2 (Supporting information), the exciton lifetimes at 620 nm were slightly decreased from 13.6 ns (without CILs) to 12.4 ns for PFN, 12.7 ns for P3PyC8-Br and 12.2 ns for P4PyC8-Br, indicating a negligible impact of these CILs on the radiative recombination of QD-R. However, for P4PyTEG-Br and P4PyTEG-TS, the exciton lifetimes were decreased to 11.0 and 11.3 ns, respectively, which reflected a more obvious exciton quenching process. In this regard, the introduction of large polarity alkoxy side chain may strengthen their moisture absorption and

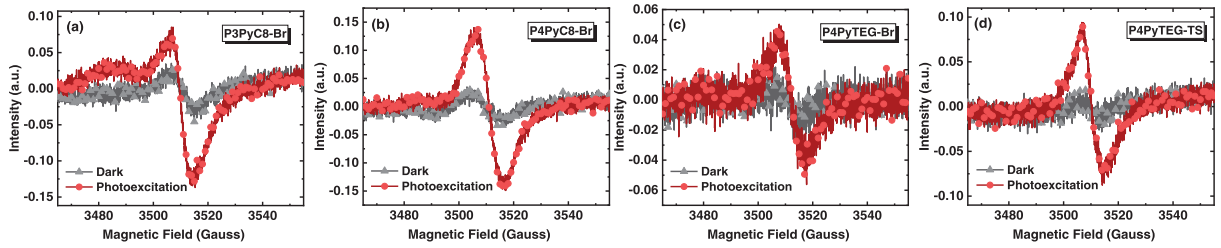

Fig. 2. EPR spectra of these polypyridinium salts measured in dark and with photoexcitation: (a) P3PyC8-Br, (b) P4PyC8-Br, (c) P4PyTEG-Br and (d) P4PyTEG-TS.

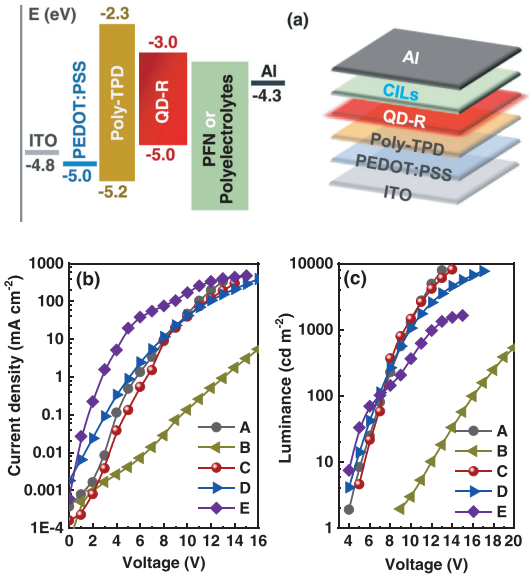

Fig. 3. (a) Schematic diagram of the QD-R based devices and energy level alignment of the devices, (b) *J-V* and (c) *L-V* characteristics of these devices.

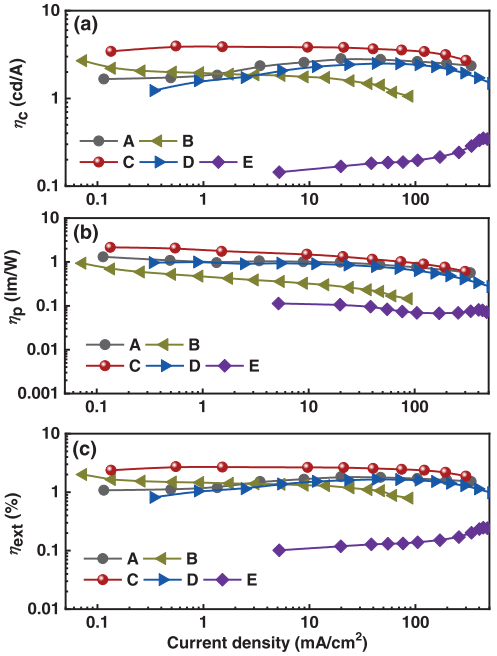

Fig. 4. (a) η_c, (b) η_p and (c) η_{ext} *versus* current density of these devices.

leading to anabatic exciton quenching. In addition, the involved QD-R demonstrated a good solvent resistance towards methanol (MeOH), and a negligible reduction of exciton lifetimes (0.13 ns) can be obtained after the treatment of MeOH, which ensured the feasibility for all-solution-processable multilayer QLED.

To evaluate the electron injection/transport property of these self-doped polypyridinium salts, all-solution-processed multilayer QLED with the architectures of ITO/PEDOT:PSS (70 nm)/Poly-TPD (10 nm)/QD-red (30 nm)/CILs (30 nm, P3PyC8-Br, P4PyC8-Br, P4PyTEG-Br and P4PyTEG-TS for device B, C, D and E, respectively)/Al (100 nm) were fabricated (Fig. 3a). As a comparison, the commercially available CILs of PFN (10 nm) was introduced and denoted as device A. The current density-voltage (*J-V*) and luminance-voltage (*L-V*) properties of these devices were depicted in Figs. 3b and c. Obviously, both devices D and E exhibited higher current density than the other three at the low operating voltage region, for example, a very high current density of 5.194 mA/cm^2 (device E) in contrast to the 0.003 mA/cm^2 (device B) at the same bias voltage of 4 V can be observed, due to the better film-forming property and lower reorganization energy of P4PyTEG-TS than P3PyC8-Br. Accordingly, the luminance of device B is remarkably lower than those of the other four devices. At the same brightness of 100 cd/m^2, the operating voltage of device B is 16.1 V, in contrast to 7.3 V of device C.

The current efficiency (η_c), power efficiency (η_p) and η_{ext} *versus* current density of these devices were shown in Fig. 4 and the detail key data were summarized in Table 1. Unexpectedly, device E demonstrated fair device performances in comparison with the device A-D, although it showed the highest current density according to the *J-V* curves, which were presumably attributed to the serious exciton quenching (Fig. S11) as well as unbalanced charge transport (Fig. 3b). Nevertheless, device C with P4PyC8-Br CILs demonstrate the best device performances with a maximum η_c, η_p and η_{ext} of 3.95 cd/A, 2.16 lm/W and 2.74%, respectively, which were respectively 1.4/1.6/1.5 times higher than those of the reference device (2.83 cd/A, 1.31 lm/W, 1.83%) with PFN as CIL. In addition, device C exhibited excellent stability with only 10% η_{ext} roll-offs even at a very high current density of 100 mA/cm^2 (Table 1). Notably, desirable CILs with self-doping feature, applicable surface morphology and polarity are essential for high-performance all-solution-processed optoelectronic devices with simplified structures, which can be feasibly realized by simultaneously modulating their anions (Br^-), N^+ positions (*para*-substituted) and side chains (alkyl) of the polypyridinium salts.

In summary, four new polypyridinium salts with self-doping feature and applicable interfacial properties were developed. Photophysical, electrochemical and DFT calculation results disclosed the significance of key molecular parameters in determining their CIL properties. All-solution-processed red QLEDs employing the self-doped CILs deliver favorable device performances, with about 50% improvements in the efficiencies compared with the device

Table 1
Key data of the QD-R based all-solution-processed devices with different CILs.

Device	CILs	L_{max}[a] (cd/m^2)	V_{ope}[b] (V)	C_{den}[c] (mA/cm^2)	η_c[d] (cd/A)	η_p[e] (lm/W)	η_{ext}[f] (%)
A	PFN	7919	7.2	0.115	2.83/1.69/2.68	1.31/1.15/0.75	1.83/1.08/1.71
B	P3PyC8-Br	931	16.1	0.003	2.69/2.07/1.04	0.94/0.57/0.15	2.00/1.50/0.81
C	P4PyC8-Br	8170	7.3	0.039	3.95/3.72/3.47	2.16/2.12/0.96	2.74/2.55/2.45
D	P4PyTEG-Br	7692	6.9	0.338	2.51/1.22/2.42	1.00/0.96/0.63	1.66/0.82/1.59
E	P4PyTEG-TS	1645	6.9	5.194	0.35/–/0.19	0.11/–/0.07	0.25/–/0.14

[a] The maximum brightness.
[b] Operating voltage at the common luminance of 100 cd/m^2.
[c] Current density under the voltage of 4 V.
[d] Current efficiency.
[e] Power.
[f] External quantum efficiency of these devices, with the sequence of maximum values, at 0.3 and 100 mA/cm^2, respectively.

with the commonly used PFN, representing one of the best results for all-solution-processed QLED with purely organic interfacial layers. This work provides a feasible strategy to design advanced CILs from self-doped polypyridinium salts.

Declaration of competing interest

The authors declare that they have no known competing financial interests or personal relationships that could have appeared to influence the work reported in this paper.

Acknowledgments

We gratefully acknowledge the financial support from the National Natural Science Foundation of China (Nos. 51803124 and 62175189), Shenzhen Science and Technology Program (Nos. KQTD20170330110107046 and JCYJ20170818143831242). The authors thank the Instrumental Analysis Center of Shenzhen University for Analytical Support. G. Xie acknowledged the funding support from the Open Project Program of Wuhan National Laboratory for Optoelectronics (No. 2019WNLOKF015) and the Open Fund of Key Laboratory for Preparation and Application of Ordered Structural Materials of Guangdong Province, Shantou University (No. KLPAOSM202003).

Supplementary materials

Supplementary material associated with this article can be found, in the online version, at doi:10.1016/j.cclet.2022.04.009.

References

[1] M. Yang, I.S. Park, T. Yasuda, J. Am. Chem. Soc. 142 (2020) 19468–19472.
[2] T. Wang, Z. Chen, H. Zhang, W. Ji, ACS Appl. Mater. Interfaces 13 (2021) 45815–45821.
[3] W. Zhang, S. Ding, W. Zhuang, Adv. Funct. Mater. 30 (2020) 2005303.
[4] H. Shen, Q. Gao, Y. Zhang, Nat. Photon. 13 (2019) 192–197.
[5] S.O. Jeon, K.H. Lee, J.S. Kim, Nat. Photon. 15 (2021) 208–215.
[6] Y. Chen, D. Zhang, Y. Zhang, Adv. Mater. 33 (2021) 2103293.
[7] J. Xue, J. Xu, J. Ren, Sci. China Chem. 64 (2021) 1786–1795.
[8] Y. Zhang, D. Zhang, T. Huang, Angew. Chem. Int. Ed. 60 (2021) 20498–20503.
[9] P. Jiang, J. Miao, X. Cao, Adv. Mater. 33 (2021) 2106954.
[10] D. Zhao, Y. Zheng, T. Meng, Sci. China Mater. 65 (2021) 757–763.
[11] Z. Wu, P. Liu, W. Zhang, K. Wang, X.W. Sun, ACS Energy Lett. 5 (2020) 1095–1106.
[12] Y. Shu, X. Lin, H. Qin, Angew. Chem. Int. Ed. 59 (2020) 22312–22323.
[13] J. Yang, M.K. Choi, U.J. Yang, Nano Lett. 21 (2021) 26–33.
[14] D. Liu, S. Cao, S. Wang, J. Phys. Chem. Lett. 11 (2020) 3111–3115.
[15] T. Kim, K.H. Kim, S. Kim, Nature 586 (2020) 385–389.
[16] M.K. Choi, J. Yang, T. Hyeon, D.H. Kim, NPJ Flex. Electron. 2 (2018) 10.
[17] Y. Ye, J. Wang, Y. Qiu, Nano Energy 90 (2021) 106583.
[18] Y. Yang, L. Su, N. Feng, Nanotechnology 32 (2021) 335203.
[19] W. Wu, Z. Chen, Y. Zhan, Adv. Mater. Interfaces 8 (2021) 2100731.
[20] J. Song, O. Wang, H. Shen, Adv. Funct. Mater. 29 (2019) 1808377.
[21] L. Wang, J. Pan, C. Liu, ACS Appl. Mater. Interfaces 13 (2021) 17861–17868.
[22] C. Xiang, L. Wu, Z. Lu, Nat. Commun. 11 (2020) 1646.
[23] B. Liu, Y. Altintas, L. Wang, Adv. Mater. 32 (2019) 1905824.
[24] H. Zhang, S. Chen, X.W. Sun, ACS Nano 12 (2018) 697–704.
[25] Y. Tang, G. Xie, X. Liang, Y.X. Zheng, C. Yang, J. Mater. Chem. C 8 (2020) 10831–10836.
[26] Y. Xiang, G. Xie, M. Huang, C. Yang, J. Mater. Chem. C 7 (2019) 13218–13223.
[27] T. Fang, T. Wang, X. Li, Sci. Bull. 66 (2021) 36–43.
[28] Y. Yu, Y. Liang, J. Yong, Adv. Funct. Mater. 32 (2022) 2106387.
[29] J.H. Kim, C.Y. Han, K.H. Lee, Chem. Mater. 27 (2015) 197–204.
[30] F. Chen, P. Lv, X. Li, J. Mater. Chem. C 7 (2019) 7636–7642.
[31] S.B. Heo, J.S. Shin, T.Y. Kim, Curr. Appl. Phys. 29 (2021) 107–113.
[32] S. Ding, Z. Wu, X. Qu, Appl. Phys. Lett. 117 (2020) 093501.
[33] Y. Tian, Z.Y. Qin, S.J. Zou, Mater. Today Energy 20 (2021) 100649.
[34] H. Feng, S. Liu, G. Tang, L. Zhang, W. Xie, J. Mater. Chem. C 9 (2021) 13748–13754.
[35] Y. Shang, Z. Ning, Natl. SSI. Rev. 4 (2017) 170–183.
[36] D.I. Son, H.H. Kim, D.K. Hwang, S. Kwon, W.K. Choi, J. Mater. Chem. C 2 (2014) 510–514.
[37] D.I. Son, H.H. Kim, S. Cho, Org. Electron. 15 (2014) 886–892.
[38] A. Castelli, F. Meinardi, M. Pasini, Nano Lett. 15 (2015) 5455–5464.
[39] X. Yin, X. Liu, Y. Peng, Adv. Funct. Mater. 29 (2019) 1806125.
[40] X. Yin, G. Xie, Y. Peng, Adv. Funct. Mater. 27 (2017) 1700695.
[41] X. Yin, G. Xie, T. Zhou, J. Mater. Chem. C 4 (2016) 6224–6229.
[42] T. Lu, F. Chen, J. Comput. Chem. 33 (2012) 580–592.
[43] R.M. Young, S.C. Jensen, K. Edme, J. Am. Chem. Soc. 138 (2016) 6163–6170.